Обзор ArXiv/astro-ph, 18-31 мая 2022

От Сильченко О.К.

Starbursts with suppressed velocity dispersion revealed in a forming cluster at $z = 2.51$

M.-Y. Xiao[1,2,3], T. Wang[1,3]⋆, D. Elbaz[2], D. Iono[4,5], X. Lu[4], L.-J. Bing[6], E. Daddi[2], B. Magnelli[2], C. Gómez-Guijarro[2], F. Bournaud[2], Q.-S. Gu[1,3], S. Jin[7,8], F. Valentino[7,9], A. Zanella[10], R. Gobat[11], S. Martin[12,13], G. Brammer[7,9], K. Kohno[14], C. Schreiber[15], L. Ciesla[6], X.-L. Yu[1,3], and K. Okumura[2]

(Affiliations can be found after the references)

May 18, 2022

ABSTRACT

One of the most prominent features of galaxy clusters is the presence of a dominant population of massive ellipticals in their cores. Stellar archaeology suggests that these gigantic beasts assembled most of their stars in the early Universe via starbursts. However, the role of dense environments and their detailed physical mechanisms in triggering starburst activities remain unknown. Here we report spatially resolved Atacama Large Millimeter/submillimeter Array (ALMA) observations of the CO $J = 3-2$ emission line, with a resolution of about 2.5 kiloparsecs, toward a forming galaxy cluster core with starburst galaxies at $z = 2.51$. In contrast to starburst galaxies in the field often associated with galaxy mergers or highly turbulent gaseous disks, our observations show that the two starbursts in the cluster exhibit dynamically cold (rotation-dominated) gas-rich disks. Their gas disks have extremely low velocity dispersion ($\sigma_0 \sim 20 - 30$ km s^{-1}), which is three times lower than their field counterparts at similar redshifts. The high gas fraction and suppressed velocity dispersion yield gravitationally unstable gas disks, which enables highly efficient star formation. The suppressed velocity dispersion, likely induced by the accretion of corotating and coplanar cold gas, might serve as an essential avenue to trigger starbursts in massive halos at high redshifts.

Key words. galaxies: clusters: general — galaxies: evolution — galaxies: formation — galaxies: high-redshift — galaxies: ISM
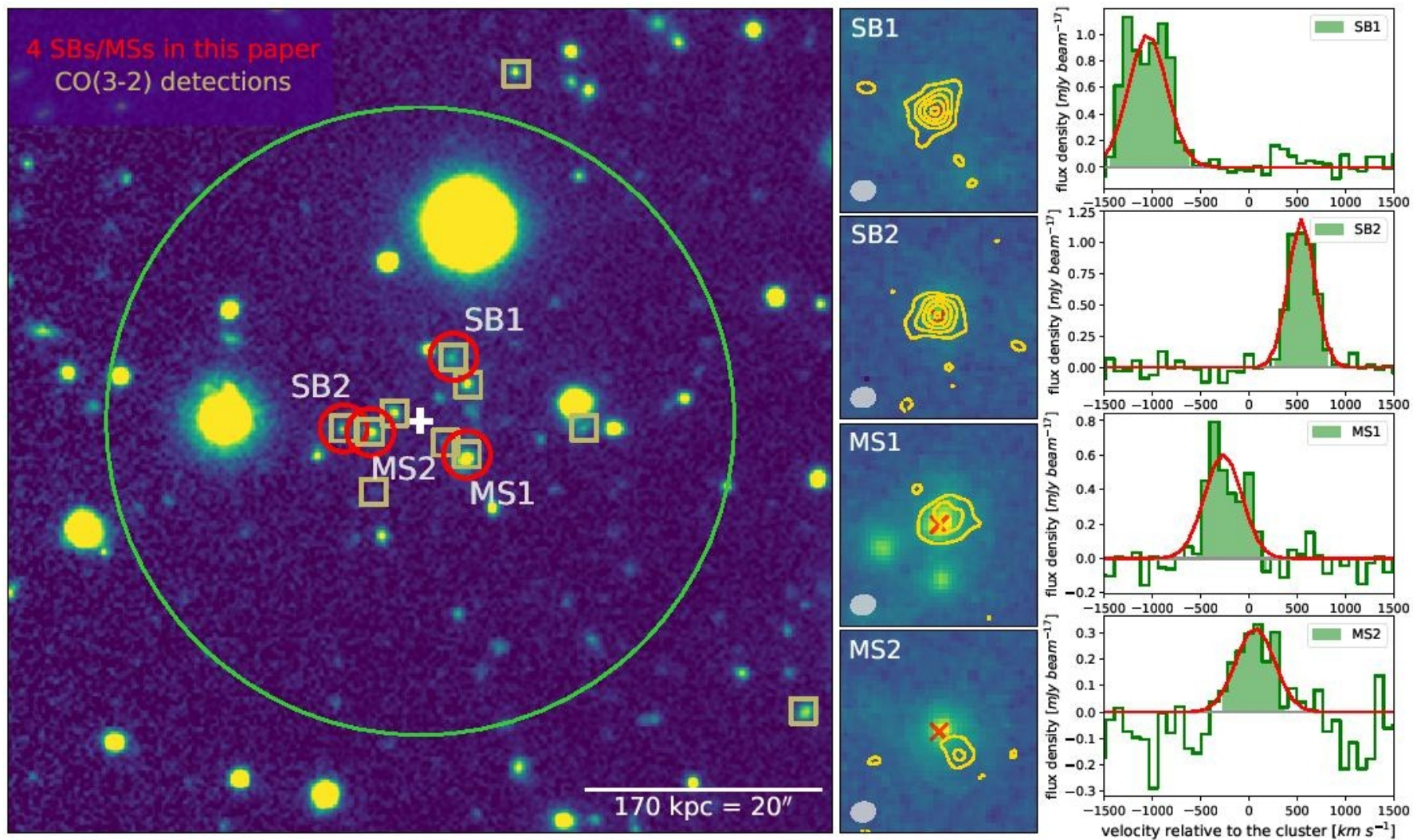
Fig. 1. Galaxy cluster CLJ1001 at $z = 2.51$ and the four member galaxies. **Left**: Sky distributions of member galaxies around the cluster center. Red circles mark the two SBs and two MSs with the brightest CO(3−2) luminosities ($S/N \gg 10$; $S/N \sim 30$ for the two SBs) among all CO(3−2) detections (golden squares) in the central region of the cluster. The background is the K_s-band image from the UltraVista survey with a size of $70''$ $\times 70''$. The white cross shows the cluster center. The scale bar indicates half of the virial radius ($R_{200c} \sim 340$ kpc) of the cluster. The large green

Table 1. Physical properties of the two SBs and two MSs in CLJ1001.

ID	^{a}ID$_{K_s}$	R.A. (J2000)	Decl. (J2000)	$z_{CO(3-2)}$	$I_{CO(3-2)}$ (Jy km s^{-1})	FWHM$_{CO(3-2)}$ (km s^{-1})
SB1	131077	10:00:56.95	+02:20:17.2	2.494	1.273 ± 0.036	547 ± 38
SB2	130891	10:00:57.56	+02:20:11.2	2.512	0.764 ± 0.028	324 ± 17
MS1	130949	10:00:56.86	+02:20:08.7	2.503	0.537 ± 0.023	453 ± 47
MS2	130901	10:00:57.39	+02:20:10.8	2.507	0.242 ± 0.024	472 ± 103

$^b\log M_*$ ($M_\odot$)	$^c\log L_{IR}$ ($L_\odot$)	^{d}SFR ($M_\odot$yr^{-1})	$^e L'_{CO(1-0)}$ (10^{10} K km s^{-1} pc^2)	$L'_{CO(3-2)}$ (10^{10} K km s^{-1} pc^2)	$^f R_{31}$	$S_{3.2mm}$ (μJy)
10.93 ± 0.15	$12.95^{+0.04}_{-0.04}$	1314 ± 122	4.9 ± 0.4	4.10 ± 0.12	0.84 ± 0.07	82 ± 10
10.83 ± 0.15	$12.70^{+0.16}_{-0.26}$	751 ± 338	3.2 ± 0.3	2.49 ± 0.09	0.78 ± 0.08	38 ± 10
11.36 ± 0.15	$12.29^{+0.16}_{-0.25}$	292 ± 128	2.3 ± 0.2	1.74 ± 0.07	0.76 ± 0.07	62 ± 12
11.35 ± 0.15	$12.30^{+0.20}_{-0.40}$	300 ± 179	1.8 ± 0.3	0.79 ± 0.08	0.44 ± 0.08	18 ± 3

$^g M_{dust}$ ($10^8 M_\odot$)	^{h}CO(3−2) Size (*UV plane*) (kpc × kpc)	^{i}CO(3−2) size (*image plane*) (kpc × kpc)	^{j}3.2 mm size (image plane) (kpc × kpc)
16.0 ± 1.5	$(2.05 \pm 0.10) \times (0.98 \pm 0.11)$	$(2.10 \pm 0.31) \times (1.43 \pm 0.32)$	$(1.87 \pm 0.54) \times (1.27 \pm 0.54)$
10.8 ± 2.2	$(1.42 \pm 0.11) \times (1.14 \pm 0.17)$	$(1.70 \pm 0.30) \times (1.40 \pm 0.32)$	(...)
8.3 ± 4.8	$(1.77 \pm 0.20) \times (1.56 \pm 0.33)$	$(2.13 \pm 0.32) \times (1.79 \pm 0.29)$	(...)
4.3 ± 1.0	$(0.79 \pm 0.20) \times (0.79 \pm 0.37)$	$(2.32 \pm 0.60) \times (0.90 \pm 0.53)$	(...)

Notes. ^{a}IDs from the K_s-selected catalog (Muzzin et al. 2013). $^b M_*$, derived from the SED fitting in W16 (scaled to a Chabrier 2003 IMF by a factor 1.7). ^{c}Total infrared luminosity, derived from the infrared SED fitting with CIGALE. ^{d}SFR, derived from L_{IR} using Kennicutt & Evans (2012) (SFR $= 1.49 \times 10^{-10} L_{IR}$; Chabrier 2003 IMF). $^e L'_{CO(1-0)}$, from W18. ^{f}CO excitation: $R_{31} = L'_{CO(3-2)}/L'_{CO(1-0)}$. $^g M_{dust}$, derived from the infrared SED fitting with CIGALE. ^{h}The best-fit semi-major and semi-minor axes of CO(3−2) in the *UV* plane. ^{i}The deconvolved semi-major and semi-minor axes of CO(3−2) in the image plane. ^{j}The deconvolved semi-major and semi-minor axes of 3.2 mm dust continuum emission in the image plane.

Повышенная доля газа = вспышка звездообразования?

Table 2. Gas properties of the two SBs and two MSs.

	SB1	SB2	MS1	MS2
[a]$\alpha_{CO}(Z)$ $(M_\odot/(K\ km\ s^{-1}\ pc^2))$	4.09	4.10	4.06	4.06
[b]$M_{gas,CO}$ $(10^{10}\,M_\odot)$	20.2 ± 1.7	13.3 ± 1.4	9.2 ± 0.9	7.4 ± 1.1
[c]$f_{gas,CO}$	$0.70^{+0.09}_{-0.06}$	$0.66^{+0.10}_{-0.07}$	$0.29^{+0.09}_{-0.06}$	$0.25^{+0.08}_{-0.06}$
[d]$t_{dep,CO}$ (Gyr)	0.15 ± 0.02	0.18 ± 0.08	0.32 ± 0.14	0.25 ± 0.15
[e]δ_{GDR}	126 ± 16	123 ± 28	110 ± 65	171 ± 47
[f]$M_{gas,GDR}$ $(10^{10}\,M_\odot)$	17.9 ± 6.4	12.8 ± 5.1	7.6 ± 5.1	4.0 ± 1.7
$f_{gas,GDR}$	$0.68^{+0.12}_{-0.10}$	$0.65^{+0.13}_{-0.11}$	$0.25^{+0.15}_{-0.14}$	$0.15^{+0.08}_{-0.07}$
$t_{dep,GDR}$ (Gyr)	0.14 ± 0.05	0.17 ± 0.10	0.26 ± 0.21	0.13 ± 0.10
[g]$M_{gas,3.2mm}$ $(10^{10}\,M_\odot)$	22.7 ± 6.4	10.4 ± 3.9	17.1 ± 5.5	5.1 ± 1.6
$f_{gas,3.2mm}$	$0.73^{+0.10}_{-0.08}$	$0.61^{+0.13}_{-0.11}$	$0.43^{+0.13}_{-0.11}$	$0.18^{+0.08}_{-0.07}$
$t_{dep,3.2mm}$ (Gyr)	0.17 ± 0.05	0.14 ± 0.08	0.59 ± 0.32	0.17 ± 0.11

Notes. The molecular gas masses are estimated based on the CO(1−0) emission line using metallicity-dependent conversion factors, gas-to-dust ratio, and 3.2mm dust continuum emission. [a]CO-to-H_2 conversion factor ($\alpha_{CO}(Z)$) from W18, calculated based on the mass-metallicity relation. [b]Total molecular gas mass, computed as $M_{gas,CO} = \alpha_{CO}(Z)L'_{CO(1-0)}$. [c]Gas fraction: $f_{gas} = M_{gas}/(M_{star} + M_{gas})$. [d]Gas depletion time: $t_{dep} = M_{gas}/SFR$, which is the inverse of the star formation efficiency (SFE = $1/t_{dep}$). [e]Gas-to-dust mass ratio, computed based on the $\delta_{GDR} − Z$ relation (Eq. 2). [f]$M_{gas,GDR}$, computed based on the gas-to-dust ratio (Eq. 1). [g]$M_{gas,3.2mm}$, computed based on the Rayleigh-Jeans tail dust continuum (Eq. 4).

Кинематика газа
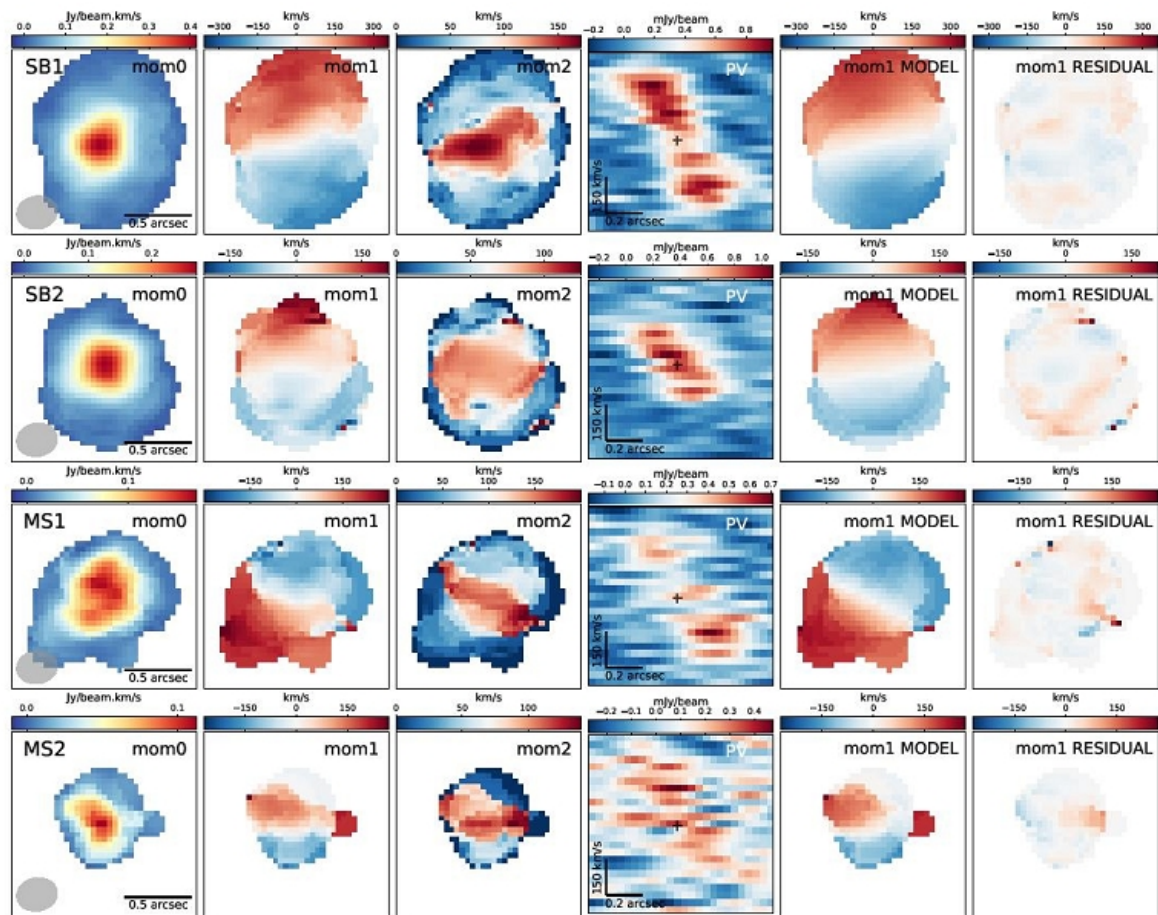
Fig. 2. CO morphology and kinematics of the four cluster members at $z = 2.51$. From left to right: ALMA maps ($1.4'' \times 1.4''$) of velocity-integrated CO(1−0) flux (*Moment* 0), velocity field (*Moment* 1), velocity dispersion (*Moment* 2), position-velocity (PV) diagrams along the major axis, the best-fit *Moment* 1 model with GalPAK^{3D}, and the residual between the data and the model. We note that these maps are without correction for beam-smearing. Gray-filled ellipses indicate the angular resolution of $0.31'' \times 0.25''$. The four member galaxies have regular rotating disks of molecular gas.

km s^{-1} pc^2)$^{-1}$; Downes & Solomon 1998; Tacconi et al. 2008) values. However, using $\alpha_{CO,SB} = 0.8\ M_\odot$(K km s^{-1} pc^2)$^{-1}$ for the two SBs would result in very low gas-to-dust ratios ($\delta_{GDR} \sim 20$), making the two SBs extreme cases. The resulting δ_{GDR} would

α_{CO}. Hence, these pieces of evidence are all consistent with our derived $\alpha_{CO}(Z)$. We however show that even if we had chosen a local SB conversion factor ($\alpha_{CO,SB} = 0.8\ M_\odot$(K km s^{-1} pc^2)$^{-1}$) for the two SBs, the main conclusions of the paper would remain

Радиальные профили
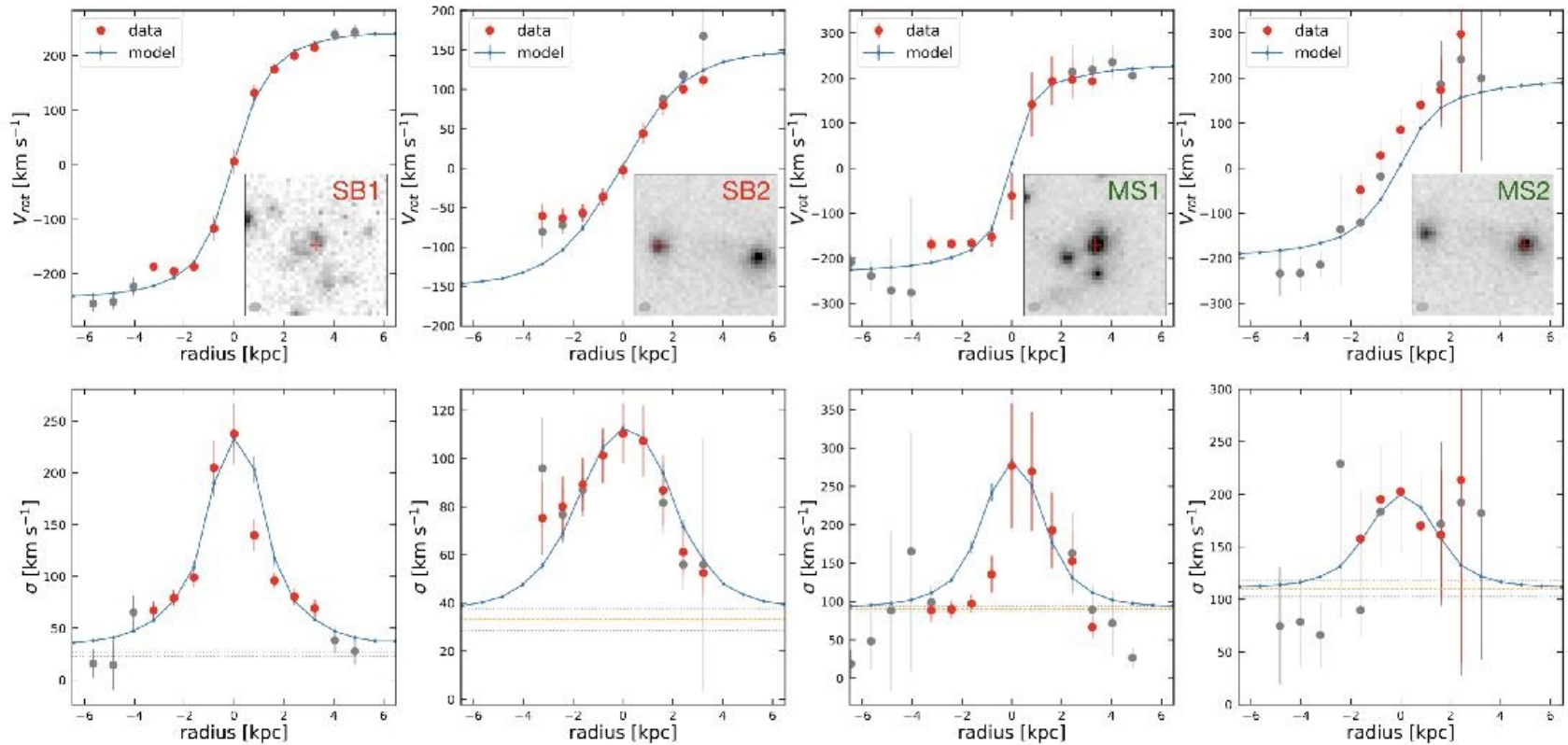
Fig. 4. Observations (points) and best-fit PSF-convolved models (blue lines) for rotation velocity and total velocity dispersion profiles along the kinematic major axis. Each point was extracted from the spectrum in an aperture whose diameter is equal to the angular resolution 0.31″ and the red one restricted to the spaxels with a S/N > 3 in the aperture. Orange and gray lines mark the intrinsic velocity dispersion σ_0 and 1σ confidence from the GalPAK^{3D}. The 3.5″ × 3.5″ *HST*/F160W images are shown in the bottom-right corner with the red crosses denote the corresponding source. Since SB2 and MS2 are close to each other with mixed fluxes, the points at the lowest radius of SB2 and the highest radius of MS2 are not fitted well with models. For MS1, the points at the lowest radius are not fitted well with models because of two neighboring sources at similar redshifts. The σ_0 derived from GalPAK^{3D} is lower than the lowest observed velocity dispersion profile because the latter one is still affected by the beam-smearing effect even at the large radii probed by our observations.

Чем интенсивнее звездообразование, тем меньше турбулентность?
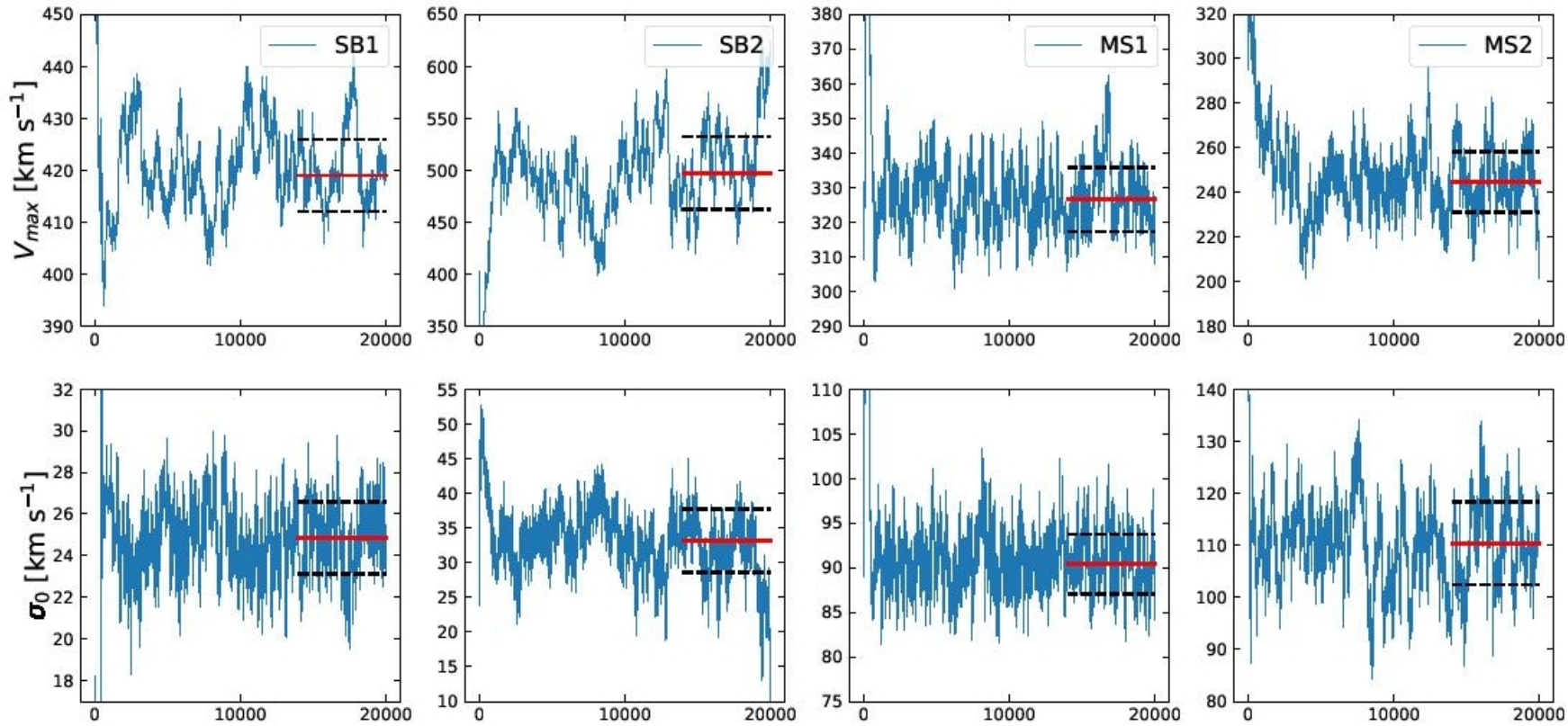
Fig. 3. Full MCMC chain for 20,000 iterations for the two SBs and two MSs. Each galaxy shows the fitting results of rotational velocity and intrinsic velocity dispersion. Red solid lines and black dashed lines refer to the median and the 1σ standard deviations of the last 30% of the MCMC chain.

Динамический статус газовых дисков
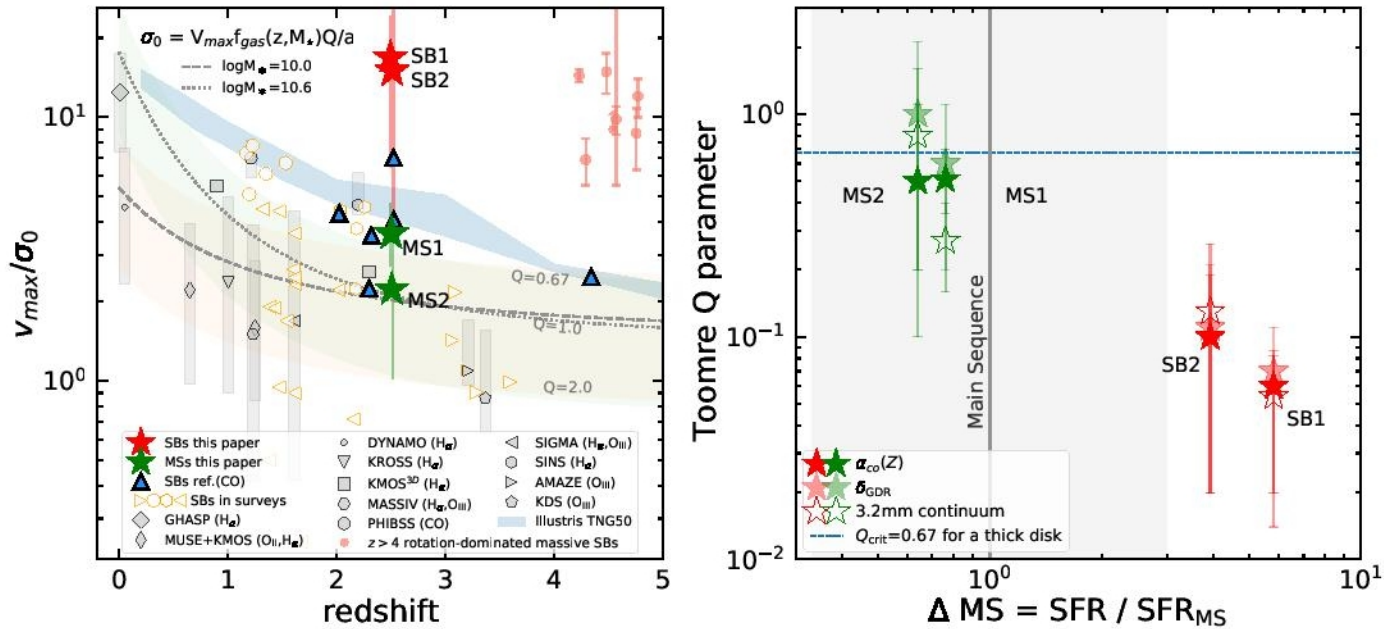
Fig. 5. Two cluster SBs have dynamically cold and gravitationally unstable gas disks. **Left**: Ratio of the gas rotational to random motion (V_{max}/σ_0) as a function of redshift, with the comparison between the two cluster SBs and two cluster MSs and samples of observed and simulated field galaxies. The two cluster SBs and two cluster MSs are in red and green stars, respectively, with uncertainties derived from our simulation (see §3.6). Filled gray symbols with vertical bars show the median values and 16-84th percentile range of field star-forming galaxies, including molecular and ionized gas detections. When possible, we identified field starbursts (orange symbols) within these literature samples at $z > 1$ as galaxies with a SFR at least 0.5 dex higher than the SFMS. Blue triangles represent field starbursts with individual CO observations (Calistro Rivera et al. 2018; Barro et al. 2017; Swinbank et al. 2011; Tadaki et al. 2017, 2019). The faint red points show massive ($M_* > 10^{10} M_\odot$) rotation-dominated SBs at $z > 4$ which have been found recently (Rizzo et al. 2020, 2021; Lelli et al. 2021; Fraternali et al. 2021), but no information on their environment is available yet. The light-blue area shows V_{max}/σ_0 values for star-forming galaxies from Illustris-TNG50 simulations in the mass range 10^9-$10^{11} M_\odot$ (Pillepich et al. 2019). The two lines with the light green and pink shaded regions describe V_{max}/σ_0 as a function of f_{gas} and Toomre Q (Wisnioski et al. 2015), where a $= \sqrt{2}$ for a disk with constant rotational velocity. **Right**: Toomre parameter Q (see §4.2) as a

Эволюция с красным смещением
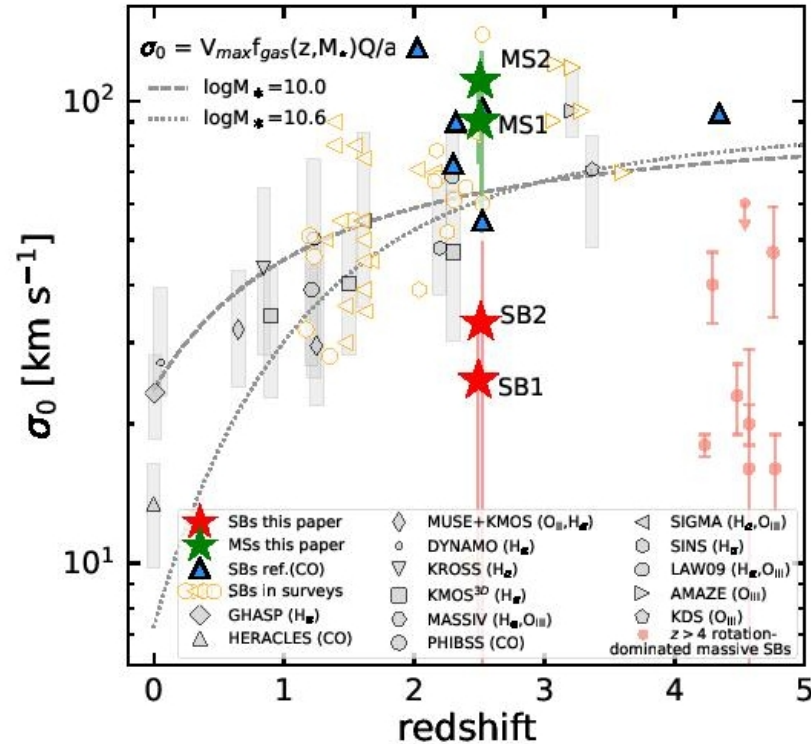
Fig. 6. Comparison of gas turbulence between the two cluster SBs and two cluster MSs and field galaxies. The intrinsic velocity dispersion increases with redshift. The symbol convention and the two lines are the same as in the left panel of Fig. 5. The two lines show the relation between the gas velocity dispersion, the gas fraction, and the disk instability for different stellar masses (Wisnioski et al. 2015). Here we assume $V_{max} = 130$ km s^{-1}, $Q = 1$, and a = $\sqrt{2}$ for a disk with constant rotational velocity. These tracks indicate that while σ_0 predictions from this relation depend on M_*, this dependency mostly vanishes at $z > 2$. The two cluster SBs have lower σ_0 than field SBs as well as most literature samples. Their uncertainties are derived from our simulation (see §3.6).